

## Novel Anode-Supported Tubular Solid-Oxide Electrolytic Cell for Direct NO Decomposition in N<sub>2</sub> Environment

Yu Tong<sup>1</sup>, Bing Zhao<sup>1</sup>, Yongli Zhao<sup>2</sup>, Tao Yang<sup>1</sup>, Fang Yang<sup>1</sup>, Qian Hu<sup>1</sup>, Chunhua Zhao<sup>1,\*</sup>

<sup>1</sup>Key Laboratory for Ultrafine Materials of Ministry of Education, School of Materials Science and Engineering, East China University of Science and Technology, Shanghai 200237, China

<sup>2</sup>College of Electronic and Electrical Engineering, Shanghai University of Engineering Science, Shanghai 201620, China

\*E-mail: [zhaochh@ecust.edu.cn](mailto:zhaochh@ecust.edu.cn)

Received: 23 March 2015 / Accepted: 30 April 2015 / Published: 27 May 2015

---

An anode-supported tubular solid-oxide electrolytic cell (AT-SOEC) for NO decomposition has been designed and fabricated successfully by dip-coating technique. The AT-SOEC comprised porous (La<sub>0.8</sub>Sr<sub>0.2</sub>)<sub>0.95</sub>MnO<sub>3</sub> (LSM95) as anode substrate, LSM95/8 mol% yttria stabilized zirconia (8YSZ) as both anode active layer and cathode layer, and 8YSZ as electrolyte. XRD patterns demonstrated that LSM95 and 8YSZ had good phase stability at 1250 °C and in NO atmosphere which indicated that they were proper electrode and electrolyte materials for NO decomposition. Electrodes with graphite powder as pore former showed uniform porosity to promote gas transmission, and the electrolyte was well densified with a thickness of less than 10 μm after sintered at 1250 °C. The designed AT-SOEC was proved to work effectively for decomposing NO (3500 ppm, balanced in N<sub>2</sub>), and results indicated that the decomposition rate of NO increased with temperature and current, and the maximum NO decomposition rate (99%) was obtained at 800 °C.

---

**Keywords:** Anode-supported; Tubular solid-oxide electrolytic cell; LSM/YSZ; NO decomposition

### 1. INTRODUCTION

Nitrogen oxides (NO<sub>x</sub>), which are mainly formed in a lean combustion engine such as diesel engine, are extremely toxic to a human body and also harmful to environment as a main source of acid rain as well as photochemical smog [1, 2]. In the past decades, a lot of efforts have been made on eliminating NO<sub>x</sub> from air, among which the catalytic decomposition was intensively concentrated [3-8]. There are mainly two categories for the catalytic decomposition methods, one is catalytic reduction method by adding NH<sub>3</sub>, H<sub>2</sub>, CO or hydrocarbon as reducing agents [3-6], the other is the direct

catalytic decomposition without reducing agents [7, 8]. However, the former may cause an inevitable secondary pollution by using toxic reducing agent. As for the latter one, despite that the reaction itself is simple and no toxic reducing agent is required, it will barely function in the presence of oxygen because most of the catalysts are deactivated in this condition, thus restricting its application in the case of lean burn that contains oxygen [7].

In 1975, Huggins et al. first reported an electrochemical way for the decomposition of NO using SOEC [9]. Since then, the electrochemical removal of NO has been intensively studied and impressive progress has been made [10-16]. Compared with other methods, the electrochemical method can work in oxygen-containing atmosphere without secondary pollution produced, thus making it an ideal candidate for the decomposition of NO [10-13]. As far as reported, the most commonly used SOEC is a multilayer planar type with electrolyte as supporting layer. Usually the supporting electrolyte layer is made thick enough ( $>500\ \mu\text{m}$ ) to reinforce the planar SOEC, which consequently obstructs the transporting of  $\text{O}^{2-}$  in electrolyte layer [14-16].

The aim of the investigation is to develop a new SOEC which not only can be operated at lower temperature, but also has commercial prospects. In the present paper, an AT-SOEC was designed and used for direct NO decomposition in  $\text{N}_2$  environment. By using anode as the supporting layer, the thickness of electrolyte layer was reduced to as thin as a few microns, which facilitates the transport of  $\text{O}^{2-}$  and lowers the operating temperature for NO decomposition. In addition, the tubular design can strengthen the whole cell, enable its steady work and cyclic utilization. At the same time, the outermost cathode which acts as the active sites of NO decomposition can be adjusted easily for possible NO selectivity.

A-site deficient LSM95 has high conductivity as well as high activity in catalytic removal of  $\text{NO}_x$ , moreover, it has similar thermal expansion coefficient and good chemical compatibility with 8YSZ electrolyte, which makes it suitable materials for electrodes [17, 18]. For this reason, LSM based electrodes have been widely used in the electrochemical reaction of  $\text{NO}_x$  [19]. In this paper, LSM95 was chosen as anode materials, 8YSZ as electrolyte, and LSM95 and 8YSZ with a weight ratio of 1:1 as anode active layer and cathode materials.

## 2. EXPERIMENTAL

### 2.1 Fabrication of AT-SOEC

Solid state reaction method was used to prepare LSM95 powder. Appropriate amounts of reagent grade powders  $\text{La}_2\text{O}_3$ ,  $\text{SrCO}_3$  and  $\text{MnCO}_3$  were weighed and mixed at room temperature in a planetary mill using zirconia balls as milling medium with a small amount of ethanol as the solvent. After drying at  $80\ ^\circ\text{C}$ , the mixture was then calcined at  $1050\ ^\circ\text{C}$  and pure perovskite phase was obtained.

The AT-SOEC was fabricated by dip-coating technique using the self-made LSM95 and commercial 8YSZ (Daiichi Kigenso Kagaku Kogyo, Japan). The preparation of the slurries for dip-coating process involved three steps. Firstly, the powders for each layer were milled in a planetary mill

for 1 h with ethanol and butanone as the solvents, and methyl ethyl ketone (MEK) as the disperse agent. To form sufficient porosity in electrodes, a certain amount of rice starch or graphite powder was added as pore former. Secondly, polyvinyl butyral and polyethylene glycol were added as binder and plasticizer, respectively, then milled for another 2 h. Finally, the slurries were vacuum pumped for about 2 min to get rid of air. The dip-coating process was carried out on a one-end-closed glass tube with an external diameter of 12 mm. First, the anode substrate layer was dipped 6 times until the thickness reached around 1mm. Following that, anode active layer was dipped against the substrate layer to enhance activity. After drying in air for about 24 h, the tube was demoulded from the glass tube and pre-sintered at 1050 °C for 4 h. Thereafter, electrolyte was dipped on the surface of anode active layer and calcined at 1250 °C for another 4 h. The last step is the coating of the outermost cathode layer and sintering at a temperature of 1100 °C.

## 2.2 Measurements

The phase composition was determined using a Bruker-D8 Advance X-ray diffractometer ( $\text{CuK}_\alpha$  radiation, 40 kV and 40 mA) at a scanning rate of  $6^\circ \text{min}^{-1}$  for detection. Overall view for the AT-SOEC was taken by a photo camera (FinePix F605EXR, FUJIFILM, Japan). The microstructure of the ceramic samples was characterized by Hitachi X-600 and S-4800 scanning electron microscope (SEM). The porosity was determined by Archimedes method in water. For electrical conducting, silver paste was adhered to the outer and inner of the tube with silver net covered evenly. To examine the tightness of the cell, helium was introduced and no gas leak was observed during the test. Then the AT-SOEC was sealed in an alumina tube with silver wires attached to anode or cathode stretching out. Current was applied by a regulated DC power supply with a digital screen showing the working current and approximate potential (APS3005Dm, ATTEN, China). Fig. 1 shows the diagram of the reactor for NO decomposition.

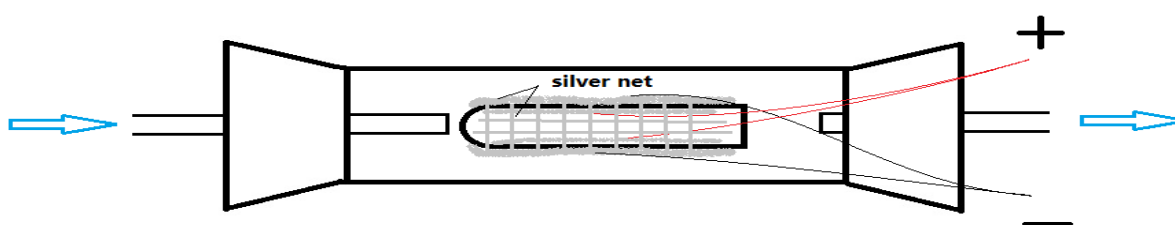


**Figure 1.** The diagram of reactor for NO decomposition.

The performance of AT-SOEC was measured from 400 °C to 800 °C by inputting gas mixture containing 3500 ppm NO (balanced in  $\text{N}_2$ ) at a flow rate of  $200 \text{ ml min}^{-1}$ . For the purpose to calculate the decomposition rate of NO, the concentrations of NO before and after reaction were detected using a  $\text{NO}_x$  gas analyzer (KM940, KANE, England).

### 3. RESULTS AND DISCUSSION

Fig. 2 gives the XRD patterns of LSM95 and 8YSZ mixture: (a) heated at 1250 °C, and (b) first heated at 1250 °C, then processed in 3500 ppm NO at a flow rate of 50 ml min<sup>-1</sup> for 10 h. As shown in Fig. 2(a), two phases are detectable according to the PDF card, that is, the rhombohedral perovskite-structured oxide (JCPDS: 89-4461) and tetragonal fluorite-structured oxide (JCPDS: 82-1243), corresponding to LSM95 and 8YSZ, respectively.

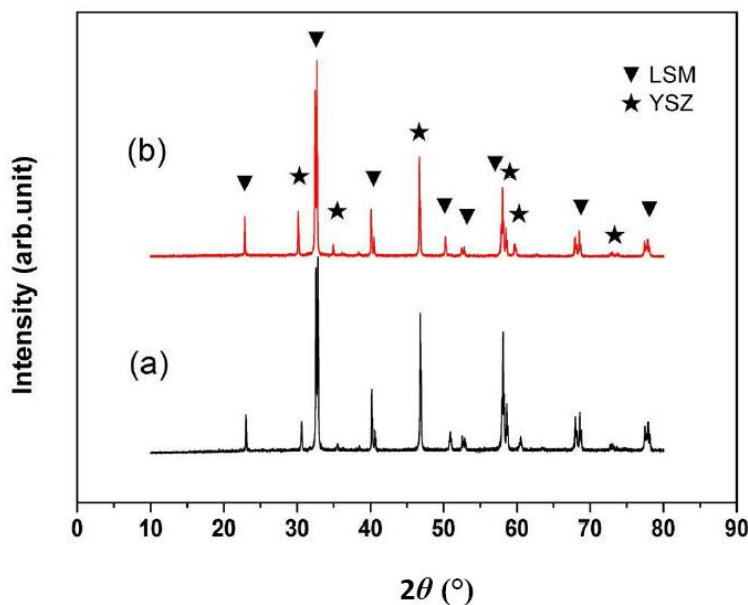


**Figure 2.** XRD patterns of LSM95/8YSZ: (a) heated at 1250 °C, and (b) first heated at 1250 °C, then processed in 3500 ppm NO at a flow rate of 50 ml min<sup>-1</sup> for 10 h.

No impurity phases, such as La<sub>2</sub>Zr<sub>2</sub>O<sub>7</sub> or SrZrO<sub>3</sub>, appeared. Using XRD, Jiang et al. observed the formation of La<sub>2</sub>Zr<sub>2</sub>O<sub>7</sub> at the interface between La<sub>0.8</sub>Sr<sub>0.2</sub>MnO<sub>3</sub> and YSZ at 1150°C [20]. It is reasonable to deduce that interface reaction between LSM95 and 8YSZ at elevated temperature of 1250°C can also be observed. However, with A-site deficient LSM95, its reaction with 8YSZ can be inhibited effectively to the extent of XRD limitation. After being processed in NO, as seen in Fig.2 (b), the XRD patterns almost remain the same without other impure phases, implying that LSM95 and 8YSZ have a good stability in the environment of NO, which is necessary for the application of NO decomposition.

Containing sufficient connected open-pores in anode and cathode is crucial for gas diffusion and NO decomposition reaction at triple phase boundaries. Adding pore former to electrodes is an effective way to improve porosity [21]. For this reason, two conventional pore formers, rice starch or graphite power, was considered for its optimization. Fig. 3 gives the SEM images of anode cross-sections sintered at 1250 °C with 20 wt% (relative to LSM95) rice starch (a) or graphite (b) powders as pore formers, respectively. The porosities are about 20 and 39 % for the anode with rice starch and graphite as pore formers respectively. The decomposition temperature and morphology of pore former

are the critical factors to decide the final porosity. The pores left by pore former at higher temperature are more easily retained during the sintering process. Table 1 gives the porosity of anode with different amounts of rice starch and graphite powder as pore formers.

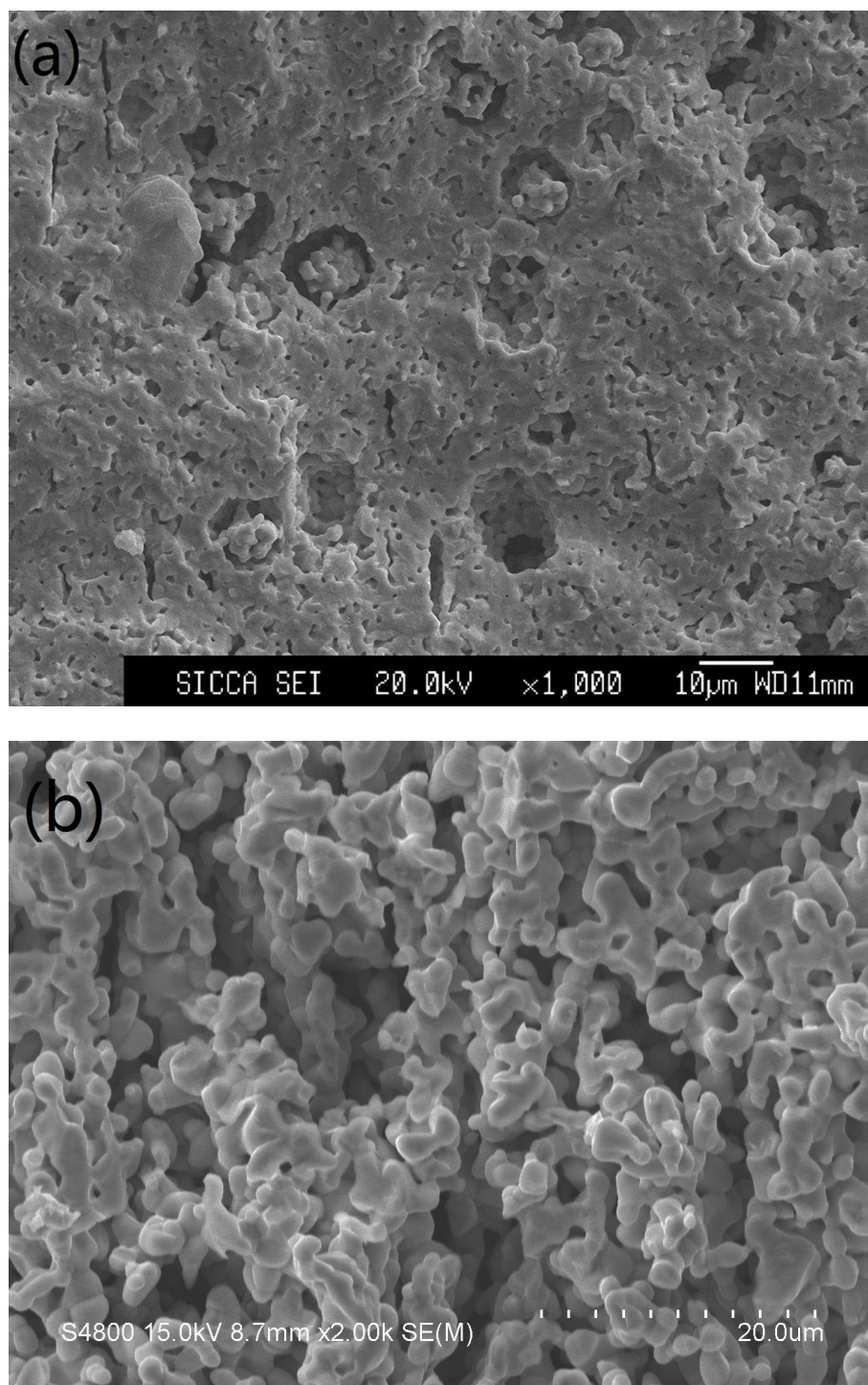
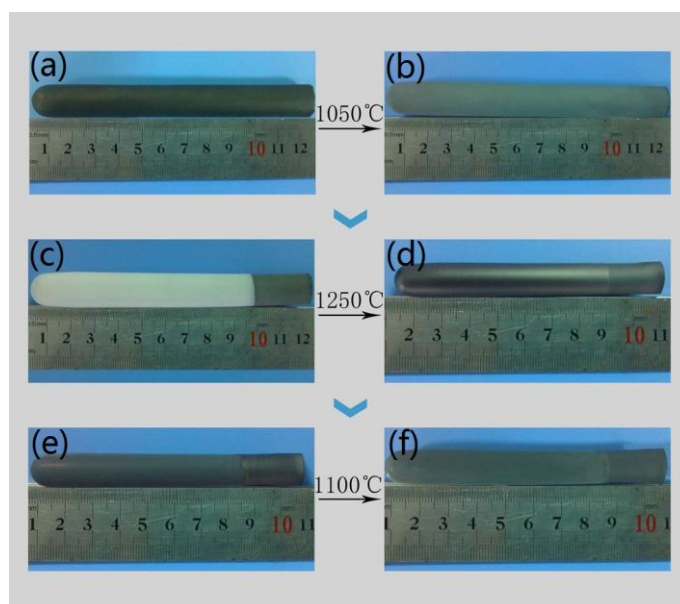


**Figure 3.** SEM images of LSM95 with rice starch (a) and graphite (b) as pore formers (20 wt% relative to LSM95 powder).

Lower porosity was shown by rice starch because the decomposition temperature of rice starch is much lower than that of graphite [22, 23]. As seen in Fig. 3, closed-pores are formed by using starch as pore former, while on the contrary, homogenous open-pores are formed by using graphite powder as pore former. Since rice starch is formed by large molecular particles with spheric shape which is hard to be broken during the ball-milling process [24], the spheric pores left by starch combustion are closed and large which are not easy to form connecting channels. On the other hand, graphite powder is formed by aggregates of nanometric particles or sub-micronic dense lamellae which can be easily broken and dispersed during the ball-milling process [24]. Then the pores left by graphite are easy to form effective connecting channels. As listed in Table 1, different amount of graphite powders were also investigated. The porosity is almost the same with 20 and 30 wt% graphite addition. But the anode substrate with 30 wt% graphite addition contains lots of flaws. And at the same time, the porosity with 10 wt% graphite addition is only 25% which is not effective for the transport of gases. Then 20 wt% graphite powder was chosen.

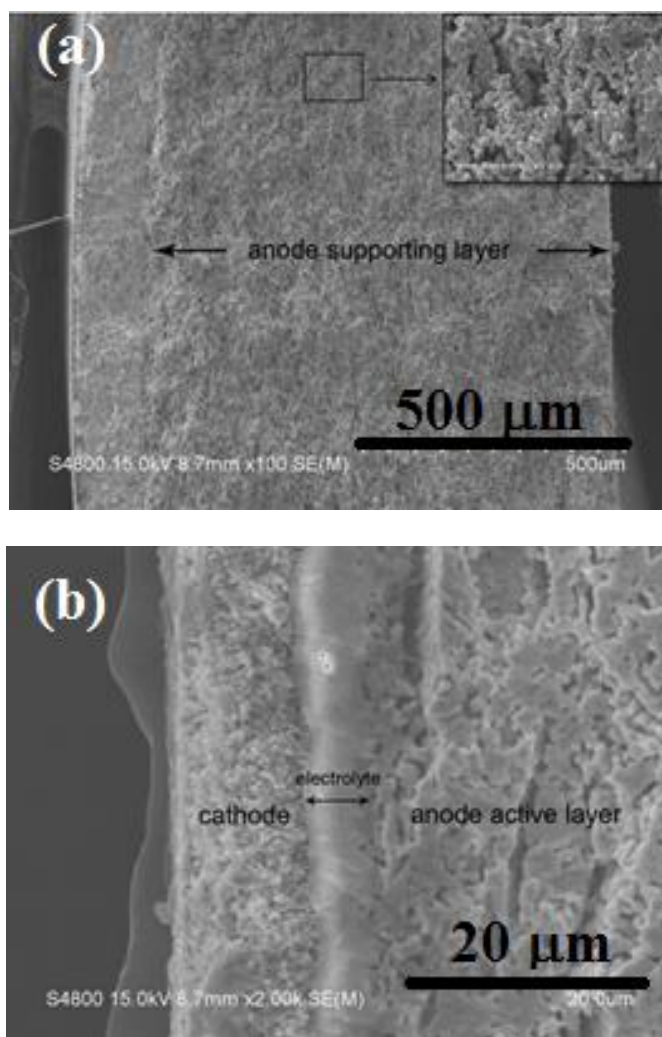
**Table 1.** The porosity of anode with different amounts of rich starch and graphite powder as pore formers

	Porosity (%)	
	Rice starch	Graphite powder
10wt%	15	23
20wt%	20	39
30wt%	22	43



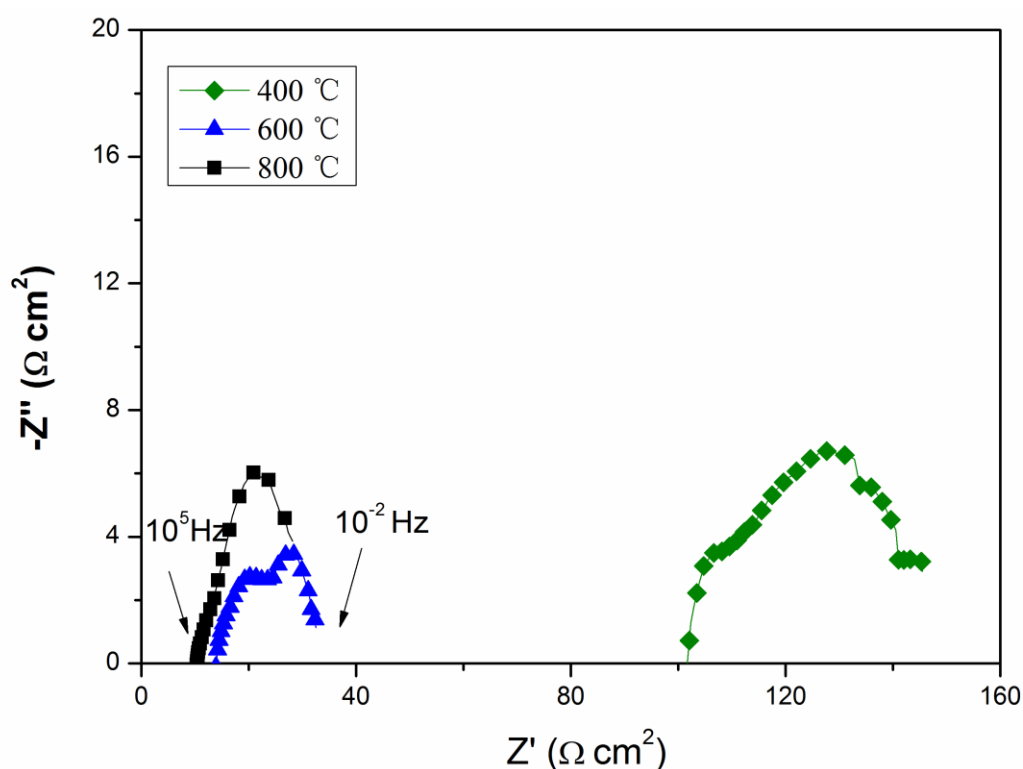
**Figure 4.** The overall view of the fabricated AT- SOEC at each stage: (a) the green anode substrate layer/anode active layer, (b) the anode pre-sintered at 1050 °C, (c) the anode/electrolyte, (d) anode/ electrolyte co-sintered at 1250 °C, (e) the anode/electrolyte/cathode, and (f) anode/electrolyte/cathode co-sintered at 1100 °C.

The overall views of the AT-SOEC at each stage are jointly shown in Fig.4. It can be seen from Fig. 4 (a) and (b), the green anode presents a perfect shape view, with a length of around 125mm, it undergoes a minimal contraction by 5 mm once pre-sintered at 1050 °C and the outer anode active layer turns to light grey in color. Comparatively, an enormous shrinkage in length can be seen while co-sintering the anode/electrolyte tube at 1250 °C, in this stage, the tube contracted by approximately 20 % with the length changes from 120 mm to 95 mm. The significant shrinkage of the tube may probably contribute to the densification of electrolytic layer [21], avoid gas leaking and meanwhile maintain high ion transfer efficiency. The additional grey active layer coated against the electrolytic layer is about 75 mm long, forming a symmetric layered structure SOEC with an outer diameter around 1.0 cm. According to the outermost active layer, the effective working area of AT-SOEC is calculated as around 24 cm<sup>2</sup>, which is much larger than that of common planar SOEC [15, 16]. The large area is beneficial for the decomposition reaction of NO.



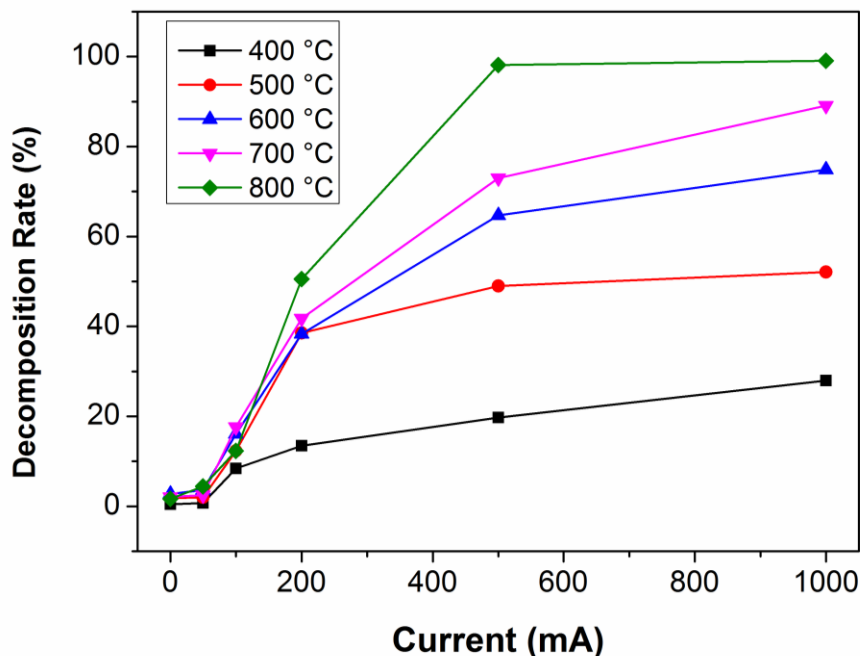
**Figure 5.** SEM images of the cross-section of the AT-SOEC after testing: (a) overview of the sandwich structure, (b) high magnification of anode active layer/electrolyte/cathode.

Fig. 5 shows the SEM photograph of the cross-section of the AT-SOEC after NO decomposition testing. On an overall scale, the electrodes show typical porous microstructure which is beneficial for the effective adsorption and transport of gases. The electrodes layers and electrolyte layer fit closely together, no cracking or delamination is observed, which further evidences that the AT-SOEC can work in a stable state. The total thickness of anode layer is about 1 mm, comprising a supporting layer around 800  $\mu\text{m}$  in thickness and an active layer which shows approximately 1/6 thickness of the supporting layer. These two layers fit well with each other so that the boundary is unobscured, and the outermost cathode is seen to be 12  $\mu\text{m}$  thick. Moreover, the electrolyte is uniform and extremely densified where only a negligible amount of closed pores can be observed, with a thickness of less than 10  $\mu\text{m}$ , the thin electrolyte layer will benefit the conductivity of  $\text{O}^{2-}$  ions [12, 21].



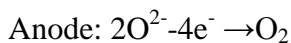
**Figure 6.** Impedance spectra of the SOEC measured under the open circuit state from 400 to 800 °C.

Fig. 6 shows the impedance spectroscopy measured under open circuit condition at different temperatures. The high frequency intercept (the left intercept of the semicircle) represents to the ohmic resistance ( $R_o$ ), involving the ionic resistance of the electrolyte, the electronic resistance of the electrode, and some contact resistance associated with interfaces. The  $R_o$  values are 102, 13.5, and 10.2  $\Omega \text{ cm}^2$  at 400, 600, and 800 °C, respectively. The low frequency intercept (the right intercept of the semicircle) corresponds to the total resistance. In general, the polarization resistance ( $R_p$ ) or reaction resistance can be given by subtracting  $R_o$  from the total resistance. It can be seen from Fig. 6 that both of  $R_o$  and  $R_p$  decreased with increasing temperature [18].



**Figure 7.** Decomposition rate curves of NO (3500 ppm, balanced in N<sub>2</sub>, at a flow rate of 200 ml min<sup>-1</sup>) as a function of current at different temperatures.

The performance for decomposing NO using the AT-SOEC is illustrated in Fig.7 and table 2. First of all, it's observable that the AT-SOEC is able to work for decomposing NO in the environment of N<sub>2</sub>. In contrast to other reports where the decomposition was carried out in rare gas atmosphere such as Ar or He [9-13], this may be more valuable for practical application. Furthermore, the NO decomposition rate increased with the increasing supplied current at all temperature. However, at relative low temperature, such as 400 °C, the growth rate is fairly slow and peak value is limited to below 25 %. When heated to higher temperature of 700 °C or 800 °C, the NO decomposition rate experiences a dramatically rapid increase and reaches the maximum of over 90%. The electrode reactions for NO decomposition are believed as below [10]:



With the current supplied to the cell, NO gas molecules stuck to the cathode acquire electrons and turn into N<sub>2</sub> and O<sup>2-</sup>. Driven by the potential force, O<sup>2-</sup> ions transfer across the solid electrolyte until getting to the anode, where electrons are released, accompanying with the generation of O<sub>2</sub> on the anode. These reactions are affected by both the electrocatalytic properties of the electrodes and the ionic conductivity of the electrolyte [9-10, 13]. At 400 °C, the ionic conductivity of electrolyte and the electrocatalytic activity of electrodes are fairly low, impeding the electrochemical reaction process. At elevated temperature, ionic conductivity of 8YSZ and the electrocatalytic activity of LSM95 are improved, thus promoting the decomposition reaction, resulting in the tremendous increase of the NO decomposition rate [13]. It is worth noting that at 800 °C, 99 % of NO gas is decomposed while providing sufficient current (>1000 mA). Normally, planer SOECs show a maximum rate just around 90 %, compared with the planar design, the tubular cell has a longer path for gas which may increase

the chance that NO molecules contact with electrons, therefore more NO gas can be decomposed [11, 18].

**Table 2.** The potential obtained with the applied current at different temperature

<i>I</i>	$U_{400^{\circ}\text{C}}$ (V)	$U_{500^{\circ}\text{C}}$ (V)	$U_{600^{\circ}\text{C}}$ (V)	$U_{700^{\circ}\text{C}}$ (V)	$U_{800^{\circ}\text{C}}$ (V)
50 mA	2.7 V	1.3 V	0.3 V	0.3 V	0.1 V
100 mA	3.3 V	1.9 V	0.9 V	0.8 V	0.6 V
200 mA	3.6 V	2.7 V	1.2 V	1.2 V	1.0 V
500 mA	4.3 V	3.5 V	2.5 V	3.0 V	2.8 V
1000 mA	4.6 V	3.9 V	4.1 V	4.0 V	3.4 V

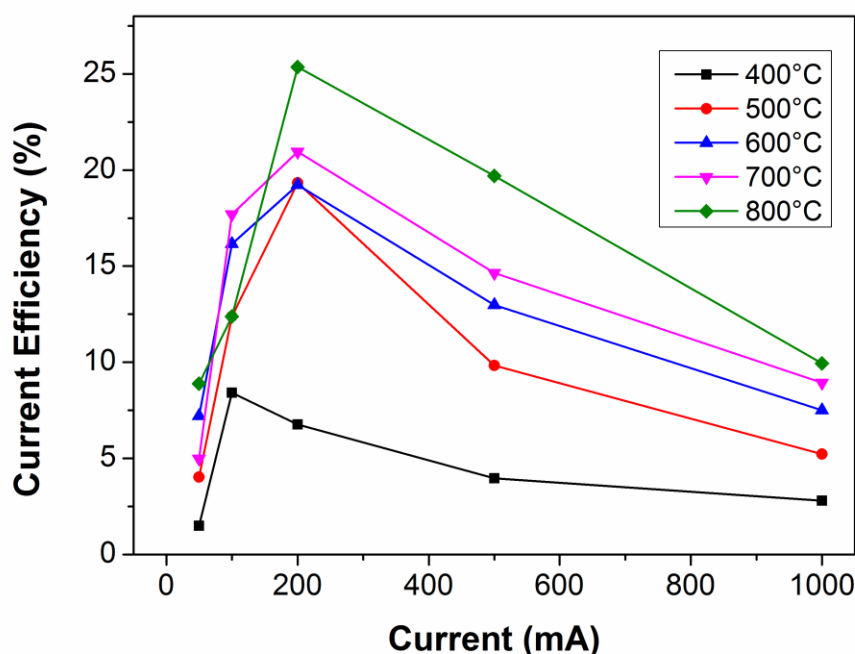


**Figure 8.** Current efficiency for NO decomposition as a function of current at different temperatures.

The line chart in Fig. 8 shows the varied current efficiency in terms of the supplied current at different temperature, which is calculated by comparing the theoretical electric charge for decomposing the certain NO and the actual one determined by the value of current. On the whole, the current efficiency increases with the temperature from 400 °C to 800 °C. In accordance with the decomposition rate curve, this should be attributed to the enhanced activity and conductivity at higher temperature. Moreover, all the current efficiency curves experience an increasing trend before hitting the peak value and then decrease constantly to the end. The low current efficiency may result from the relative low utilization rate of current. As NO gas just flows through the tube rather than remain in it, sufficient current should be provided in order to enhance the contacting opportunity between NO

molecules and electrons. However, quite amount of current is wasted in this case (e.g. current leakage) [13], and this is aggravated when the supplied current further increases, leading to the relative low current efficiency despite of the constant rising decomposition rate. It is clear that the peak value of current efficiency appears at 100 mA when temperature is low (400 °C) and shift to 200 mA at higher temperatures. The maximum utilization rate of current is about 26% at 800 °C.

#### 4. CONCLUSIONS

A novel AT-SOEC for the electrochemical decomposition of NO was designed, and the AT-SOEC with perfect shape was successfully fabricated. Rice starch and graphite powder as pore formers for fabricating AT-SOEC were compared and SEM images indicated that graphite powder was more appropriate. XRD patterns and SEM images demonstrated that AT-SOEC maintained stable during the process of NO decomposition. It's worth stressing that the AT-SOEC is proved to work effectively for direct NO decomposition in an environment of N<sub>2</sub> with the considerable high decomposition rate. However, the current efficiency is still unsatisfactory at lower temperature, next we will try to enhance the efficiency by adjusting electrolyte or electrode materials, moreover, the adding of different adsorption layers will also be a focus to pursue high efficiency and selectivity decomposition of NO in O<sub>2</sub> containing environment.

#### ACKNOWLEDGEMENTS

This work is supported by National Natural Science Foundation of China (Grant no.: 51102094), the Fundamental Research Funds for the Central Universities (Grant no.: WD1214067), Research Fund for the Doctoral Program of Higher Education of China (Grant no.: 20110074120013), Shanghai Leading Academic Discipline Project (Grant no.: B502), Shanghai Key Laboratory Project (Grant no.: 08DZ2230500), and Foundation for University Young teachers of Shanghai.

#### References

1. M. T. Lerda, J. W. Munger, D. J. Jacob, *Science* 289 (2000) 2291.
2. B. J. Finlayson-Pitts, J. N. Pitts Jr, *Science* 276 (1997) 1045.
3. W. F. Libby, *Science* 171 (1971) 499.
4. Y. Nishihata, J. Mizuki, T. Akao, H. Tanaka, M. Uenishi, M. Kimura, T. Okamoto, N. Hamada, *Nature* 418 (2002) 164.
5. Q. Zhang, X. Liu, P. Ning, Z. Song, H. Li, J. Gu, *Catal. Sci. Technol.* 5 (2015) 2260.
6. T. Chaieb, L. Delannoy, S. Casale, C. Louis, C. Thomas, *Chem. Commun.* 51 (2015) 796.
7. F. Garin, *Appl. Catal. A: Gen.* 222 (2001) 183.
8. K. Miura, H. Nakagawa, R. Kitaura, T. Satoh, *Chem. Eng. Sci.* 56 (2001) 1623.
9. S. Pancharatnam, R. A. Huggins, D. M. Mason, *J. Electrochem. Soc.* 122 (1975) 869.
10. T. M. Gur, R. A. Huggins, *J. Electrochem. Soc.* 126 (1979) 1067.
11. S. Park, H. S. Song, H. J. Choi, J. Moon, *Solid State Ionics* 175 (2004) 625.
12. K. Hamamoto, T. Suzuki, Y. Fujishiro, M. Awano, *J. Electrochem. Soc.* 158 (2011) B1050.
13. T. Hibino, *Chem. Lett.* 5 (1994) 927.
14. S. Bredikhin, K. Hamamoto, Y. Fujishiro, M. Awano, *Ionics* 15 (2009) 285.

15. M. Awano, S. Bredikhin, A. Aronin, et.al. G. Abrosimova, S. Katayama, T. Hiramatsu, *Solid State Ionics* 175 (2004) 605.
16. S. Bredikhin, G. Abrosimova, A. Aronin, K. Hamamoto, Y. Fujishiro, S. Katayama, M. Awano, *J. Electrochem. Soc.* 151 (2004) 195.
17. T. Tsai, S. A. Barnett SA, *Solid State Ionics* 93 (1997) 207
18. H. J. Hwang, J. W. Moon, M. Awano, *Mater. Res. Bullet.* 38 (2003) 311.
19. J. Shao, K. K. Hansen, *Electrochimica Acta* 90 (2013) 482.
20. S. P. Jiang, J. P. Zhang, Y. Ramprakash, D. Milosevic, K. Wilshier, *J Mater. Sci.* 35 (2000) 2735.
21. Y. X. Shi, N. S. Cai, C. Li, C. Bao, E. Croiset, J. Q. Qian, Q. Hu, S. R. Wang, *J. Power Sources* 172 (2007) 235–245.
22. Y. Liu, S. Hashimoto, H. Nishino, K. Takei, M. Mori, *J. Power Sources* 174 (2007) 95.
23. F. A. Almeida, E. C. Botelho, F. C. L. Melo, T. M. B. Campos, G. P. Thim, *J. Eur. Ceram. Soc.* 29 (2009) 1587.
24. A. Sanson, P. Pinasco, E. Roncari, *J. Eur. Ceram. Soc.* 28 (2008) 1221.

© 2015 The Authors. Published by ESG ([www.electrochemsci.org](http://www.electrochemsci.org)). This article is an open access article distributed under the terms and conditions of the Creative Commons Attribution license (<http://creativecommons.org/licenses/by/4.0/>).